A 3-D Dual-Polarized Near-Field Microwave Imaging System

Mohammad Asefi, *Student Member, IEEE*, Majid OstadRahimi, *Member, IEEE*, Amer Zakaria, *Member, IEEE*, and Joe LoVetri, *Senior Member, IEEE*

***Abstract*—A novel 3-D dual-polarized microwave imaging system based on the modulated scattering technique (MST) is presented. The system collects the magnitude and phase of the scattered field using 120 MST probes and 12 transmitter/collector antennas distributed around an object-of-interest in the near-field region. The 12 antennas form a middle circumferential layer while the printed MST probes are arranged on three circumferential layers including the middle layer. The antennas are linearly polarized double-layer Vivaldi antennas, each fixed inside its own cylindrical conducting cavity and slanted with respect to the vertical axis of the imaging chamber. The MST probes are etched on both sides of a thin substrate and loaded with five evenly distributed p-i-n diodes along their length. These are positioned vertically and horizontally so that the z- and ϕ-components of the electric field is measured. Field data are collected using MST, calibrated, and then inverted using a multiplicatively regularized finite-element contrast source inversion algorithm. The system performance is evaluated by collecting and inverting data from different 3-D targets.**

***Index Terms*—Contrast source inversion (CSI) inverse scattering problems, finite-element method (FEM), microwave imaging (MWI), modulated scattering technique (MST), 3-D imaging.**

I. Introduction

THE USE of microwave imaging (MWI) to noninvasively estimate the dielectric properties within an object-of-interest (OI) is an alternative as well as a complementary option to existing imaging modalities. MWI is relatively low cost, portable, and uses nonionizing microwave radiation (for biomedical applications, frequencies in the range of 1–6 GHz are used). The objective of MWI is to obtain a dielectric "map" of an OI providing qualitative information regarding the shape and location of the OI's internal features, as well as some quantitative electromagnetic properties of those features [1], [2]. It has been applied to various civil, military, and biomedical imaging applications, e.g., see [3]–[10], and the references therein. Biomedical imaging is the main motivation for the work presented herein.

Manuscript received February 10, 2014; revised April 14, 2014 and May 22, 2014; accepted June 13, 2014. Date of publication July 11, 2014; date of current version August 04, 2014. This work was supported by the Natural Sciences and Engineering Research Council (NSERC) of Canada.

The authors are with the Department of Electrical and Computer Engineering, University of Manitoba, Winnipeg, MB, Canada R3T 5V6 (e-mail: Joe_LoVetri@umanitoba.ca).

Color versions of one or more of the figures in this paper are available online at http://ieeexplore.ieee.org.

Digital Object Identifier 10.1109/TMTT.2014.2333497

An MWI system typically consists of antennas, a data acquisition system, and a post processing unit, which is required to calibrate and invert the collected data so as to create the required image. Most MWI systems that have been investigated in the past can be categorized into two types. Radar-based MWI systems typically locate strong scattering regions within the OI [11]. Data acquisition for such systems consists of collecting wideband scattering data at several different locations, using either a single antenna [12] or an array of antennas [13]. Image reconstruction for such systems does not incur a heavy computational cost compared to the second category of systems, which implement full nonlinear inverse scattering techniques to create quantitative images. These latter methods, sometimes referred to as microwave tomography (MWT) when imaging a 2-D cross section of the OI, require the collection of large amounts of scattered-field data. Due to the fact that quantitative information of the dielectric properties is to be reconstructed, collecting data at different frequencies is usually not effective for OIs containing materials that vary substantially with frequency (e.g., in biomedical imaging applications). Thus, the large amount of scattered-field data that is required for these methods is collected using a large number of transmitter and receiver locations. Additional data can also be obtained by accurately measuring the different polarizations of the scattered field.

Performing near-field measurements accurately, while keeping the corresponding inversion model complexity manageable can be quite difficult, and with few exceptions, the majority of previously developed MWI systems have only transmitted and collected a single polarization of the microwave field circumferential around the OI in a 2-D plane [14], [15].

MWT systems have been evolving towards fully 3-D MWI systems, but to the authors' knowledge, no multi-polarized fully 3-D near-field imaging systems have been reported (i.e., those where multi-polarized scattered-field data are collected in the near-field to form 3-D quantitative images). The challenges of developing fully 3-D MWT systems have been addressed via several approaches in the past. Near-field 3-D data have been collected by mechanically moving the level of the antennas of a 2-D MWT system [16]; even though the data collected using this technique are 2-D, they can be manipulated and inverted using a 3-D inversion algorithm [17]. Although the system reported in [18] and [19] is a 3-D system, it collects only the ϕ-component of the electric field to reconstruct 3-D images. Another approach involves using one transmitter and one receiver rotated around the OI in a cylindrical fashion; at

each transmitter location, the receiver is mechanically moved to collect fields at equally separated measurement points [20]. A third approach, described in [21], consists of two antennas: a transmitter moving in a spherical pattern around the OI, and a receiver repositioned at equidistant points in a single 2-D plane; the measurements are performed in an anechoic chamber in the far-field region of the antennas. The common feature between the three aforementioned systems is that the collected electric field is polarized along the z-direction; it should be noted that in [21] the polarization of the transmitter changes, but not that of the receiver.

The only reported dual-polarized near-field system is a 2-D MWT system, which collects the z- and ϕ-polarizations in a single 2-D cross-sectional plane to form 2-D tomographic images [22]. Here we introduce a novel MWI system, significantly improving this 2-D multi-polarized system, that is capable of fully 3-D MWI using scattered-field data collected in two polarizations via scattered-field probes similar to those used in implementations of the modulated-scattering technique (MST) [23]–[27]. Here we refer to these probes as MST probes, although, the "modulation" is effected using differential S_{12} measurements with a vector network analyzer (VNA), as in [22] and [28]. In this paper, these differential S_{12} measurements are denoted by the variable U. We show that the extension to 3-D can be achieved by adding MST probes to two additional circumferential layers in the chamber while keeping the number of transmitter and collector antennas the same as in the 2-D system. That is, in the MWI system described herein the total number of microwave antennas is 12. The use of MST probes as receiver points on additional circumferential layers provides sufficient data for successful 3-D imaging while keeping the number of microwave ports to a minimum. This reduces the overall cost and size of the MWI system.

The dual-polarized 3-D data is collected using fast switching circuits with fixed antennas and MST probes that require no mechanical movement. Two electric-field polarizations, z and ϕ, are collected at the probe locations. The system's transmitter and collector antennas are located in a middle circumferential layer, with the field-probes distributed evenly in three circumferential layers including the middle layer. This setup allows a large number of field-probe measurement locations to be accommodated (120 probes at 60 locations in the present case).

In addition to developing this novel 3-D system, we have also studied the use of two inversion models with corresponding calibration techniques that help to mitigate the so-called modeling error in the inversion while keeping computational costs manageable. In the first inversion model, the transmitting antennas of the MWI system are modeled using a single Hertzian dipole, while the second utilizes two dipoles strategically placed within a conducting cylinder. Scattered field calibration techniques [29] are used to calibrate the measurement data for either inversion model.

This paper is organized as follows. A detailed description of the setup, as well as the data calibration are outlined in Section II. The system modeling discussion and inversion results are presented in Section III. Finally, the paper is concluded in Section IV.

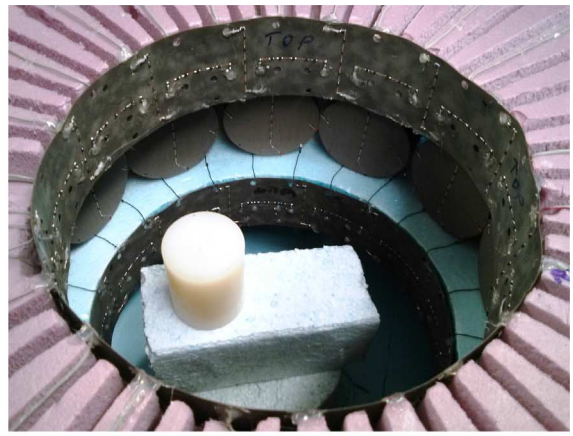

(a)

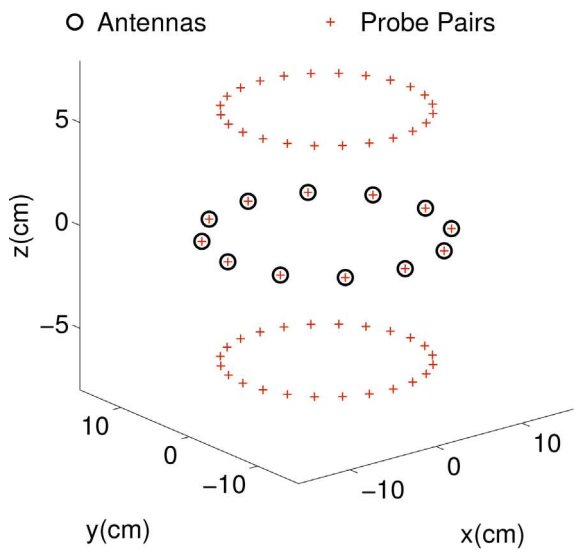

(b)

Fig. 1. (a) 3-D MWI system with a nylon cylinder target. (b) Depiction of the antennas' and probe-pairs' locations.

II. System Description

A photograph of the measurement system is shown in Fig. 1(a). 12 cavity-backed doubled-layered Vivaldi antennas (DLVAs), evenly positioned on a circle of 11.5-cm radius, are mounted on a Plexiglas cylinder. The antennas are connected to a 2×12 microwave switch multiplexer, which is also connected to a two-port VNA. Each antenna illuminates the OI successively, while the remaining antennas collect the field based on the MST [28]. The MST field probes are distributed around the OI on three different layers. The scattered field by the probes is collected by the collector DLVA antennas and its phase and magnitude is stored in a computer through the VNA since the probes are used as scatterers and are not modulated. The system's receiver module and its block diagram are discussed in detail in [22].

A. DLVA-Cavity Antennas

Each linearly polarized DLVA is mounted at a 45° angle with respect to the z-axis within its own cylindrical cavity. This composite assembly operates in a similar manner to a dual-mode

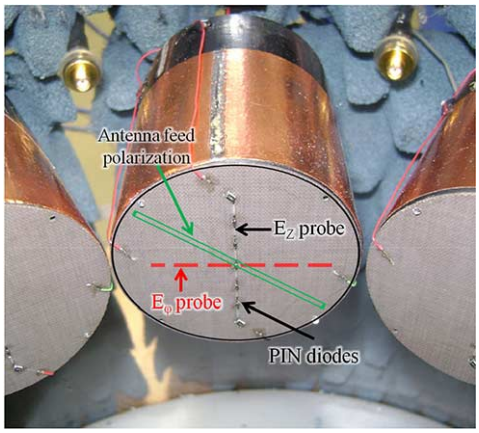

Fig. 2. DLVA antenna and its probes orientation.

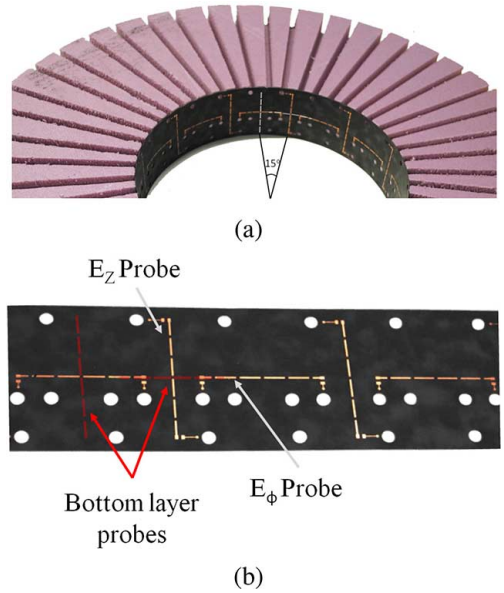

Fig. 3. (a) Styrofoam support. (b) Printed probes.

circular horn antenna with the TE_{11} and TM_{11} modes being predominantly excited. The metallic cavity "hides" the biasing wires of the MST probes, substantially reducing unwanted interferences. Fig. 2 illustrates a DLVA-cavity assembly with an MST probe pair mounted at its aperture. The slant orientation of the DLVA is similar to our dual-polarized 2-D system [22], which enables the system to illuminate the OI simultaneously with both the horizontal $(\phi-)$ and vertical $(z-)$ polarizations. These DLVA-cavity antennas have been analyzed and described in detail in [30].

B. MST Probes

Three layers of MST probe pairs constitute the field measurement locations, as shown in Fig. 1. The probes are half-wavelength at approximately 3.75 GHz (4 cm). Each probe pair consists of a vertically oriented, as well as a horizontally oriented probe, on either side of the substrate, which are used to indirectly measure the z- and ϕ-electric-field components (E_z and E_ϕ) using MST. That is, on each printed wire probe five equally spaced p-i-n diodes are soldered in series and can be forward or reverse biased using biasing wires connected to a probe-driver circuit, which precisely controls the biasing current. The forward and reverse biasing of these diodes effectively turns the probe "on" and "off" with the differential scattering being measured using the nearest DLVA.

The middle layer has 12 probe pairs, while the lower and upper layers have 24 pairs each. The middle layer is considered to be located in the $z = 0$ plane, while the lower and upper layers are positioned at $z = \{-6.1, 6.1\}$ cm. The probes in the middle layer are evenly distributed on a circular circumference of radius 11.5 cm; the probes in the lower and upper layers are uniformly spaced on a circular circumference of 9.75-cm radius. For the middle layer, the probes are etched on either sides of a circular-disc substrate that is fixed to the aperture of the cavity-backed DLVAs, as shown in Fig. 2. During a measurement, the probe pair in front of the transmitting antenna remains unbiased or "off" to allow the antenna to radiate efficiently. As for the other two layers, the probe pairs are etched on a thin flexible RT-Duroid substrate that can bend easily to take on a circular form, as shown in Fig. 3(a). The locations of the probe pairs with respect to the position of the antennas are depicted in Fig. 1(b).

The aforementioned three-layer configuration of probes in this system enables the collection of more measurements in two different field polarizations without adding more microwave switching circuitry. Furthermore, at a single frequency, the number of measurement points per dataset is $59 \times 12 \times 2 = 1416$. The total time required to measure a complete dataset for a single frequency is less than 1 min.

To accommodate the biasing wires without lengthening each probe, several holes are drilled on the substrate at the location where the biasing wires are soldered to the probes. This ensures that the length of probes along the z- and ϕ-axes does not "look" longer than the designed length. Moreover, to hold the substrate in place and properly keep the biasing wires transverse to the plane of the probes, and to reduce unwanted perturbation of the field inside the chamber by the biasing wires, a Styrofoam support was made, as illustrated in Fig. 3(a). A detailed description of the design of the probes has been presented in [22].

C. Calibration

In order to utilize the MST measurements in an inversion algorithm, the data collected for each OI must be calibrated to better correspond to the inversion model and thereby reduce the imaging system's modeling error. Generally, a known reference object is used for calibration as long as it can be accurately modeled (both shape and electrical properties). The details of this "scattered-field calibration" procedure have been described in [14], [22], [28], and [29] and are outlined briefly here.

For calibrating the data for a specific OI, three datasets are collected, which are: 1) the incident-field measurements with an empty chamber (U^{inc}), i.e., in the absence of any object inside the imaging region; 2) the total-field measurements in the presence of a reference object $(U^{\mathrm{tot,ref}})$; and 3) the total-field measurements in the presence of an OI $(U^{\mathrm{tot,OI}})$. Once these

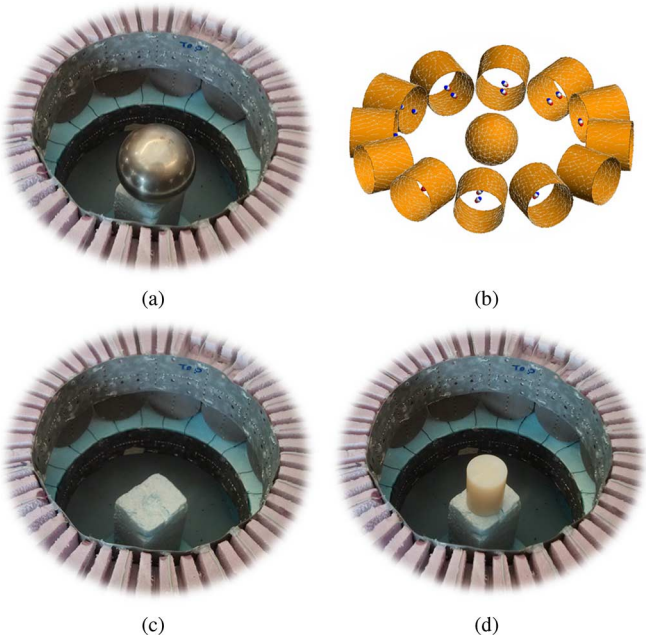

Fig. 4. Measurement and simulation settings to collect: (a) $\{U^{\mathrm{tot,ref}}_{z,t,p}, U^{\mathrm{tot,ref}}_{\phi,t,p}\}$ for reference object, (b) $\{E^{\mathrm{tot,ref}}_{z,t,p}, E^{\mathrm{tot,ref}}_{\phi,t,p}\}$ for reference object, (c) $\{U^{\mathrm{inc}}_{z,t,p}, U^{\mathrm{inc}}_{\phi,t,p}\}$ for empty chamber, and (d) $\{U^{\mathrm{tot,OI}}_{z,t,p}, U^{\mathrm{tot,OI}}_{\phi,t,p}\}$ for OI.

measurements are performed, a set of calibration coefficients are calculated for the system, where each coefficient is dependent on the field polarization and the locations of the transmitter and the probe. The calibration coefficient for the v-component of a scattered field measured at the pth probe due to a field excited by the tth transmitter is given as

$$\mathrm{CF}_{v,t,p} = \frac{E^{\mathrm{sct,ref}}_{v,t,p}}{U^{\mathrm{tot,ref}}_{v,t,p} - U^{\mathrm{inc}}_{v,t,p}}. \tag{1}$$

Here, $E^{\mathrm{sct,ref}}_{v,t,p}$ is the scattered field due to the reference object that can either be calculated analytically or evaluated using a numerical algorithm. The reference object used in the imaging study presented herein is a 3.75-cm radius metallic sphere positioned at the center of the system (due to ease of modeling and its well-defined scattering properties).

Next, each collected dataset for a given OI is calibrated using the aforementioned coefficients as follows:

$$E^{\mathrm{sct,cal}}_{v,t,p} = \mathrm{CF}_{v,t,p} \cdot \left(U^{\mathrm{tot,OI}}_{v,t,p} - U^{\mathrm{inc}}_{v,t,p} \right). \tag{2}$$

The calibrated data are used by the inversion algorithm.

The different measurement and simulation settings for collecting data utilized in the calibration procedure are illustrated in Fig. 4.

III. Models and Results

The geometry of the DLVA-cavity assembly is too complicated to be included in the numerical inversion model. Including such a complicated antenna into the inversion model would significantly increase the computational burden and considerably slow down the image reconstruction. Here we describe two simplified antenna models that have been studied and implemented to effectively manage this complexity.

In the first approach, each DLVA-cavity assembly is simply modeled as a Hertzian dipole oriented parallel to the DLVA. Although the radiation characteristics of a Hertzian dipole are different than that of DLVA-cavity assembly, we have shown in [29] that a suitable calibration technique, e.g., the technique described in Section II-C, can sometimes compensate for the resulting modeling error.

In the second approach, we incorporate a slightly more sophisticated antenna model into the inversion algorithm to further reduce the resulting modeling error. Due to the similarity between a DLVA-cavity assembly and a dual-mode circular horn antenna, we utilize a simplified model wherein two dipole antennas are strategically placed inside a metallic circular cylinder. Proper positioning of the dipoles is used to effectively excite the same amount of TE_{11} and TM_{11} modes as those in the physical DLVA-cavity assembly.

In this section, the two approaches are evaluated and compared by using each to calibrate and invert the same datasets collected from the MWI system. Data for two OI configurations, depicted in Fig. 6, are measured and calibrated. Next, the datasets were inverted using a parallelized multiplicatively regularized finite-element contrast source inversion algorithm (MR-FEM-CSI) [31]. For each dataset, the inversion algorithm was run for 150 iterations to ensure convergence. The imaging domain, $\mathcal{D}$, was selected to be a sphere of 10-cm radius centered at the origin. The number of unknowns located inside the imaging domain is $\approx 57\,000$ elements. The inversion mesh had 418 634 tetrahedral elements and 499 402 unique edges. With the algorithm running on 32 cores, the time per iteration was $\approx$ 48 s. The overhead time for the algorithm was 741 s. The average memory utilized per core was $\approx$ 700 MB primarily devoted to store the inverse finite-element method (FEM) operator. Further details regarding the inversion algorithm can be found in [31].

A. Hertzian Dipole Model

In the first utilized model, the transmitting antennas are modeled as infinitesimal Hertzian electric dipole sources with current densities composed of ϕ and z components, as shown in Fig. 5(a). For an electric dipole t located at $\vec{r}_t = (x_t, y_t, 0)$, its current density is given as

$$\begin{aligned} \vec{J}_t &= \frac{1}{\sqrt{2}}(\hat{\phi} + \hat{z}) \\ &= \frac{1}{\sqrt{2}}(-\sin(\phi_t)\hat{x} + \cos(\phi_t)\hat{y} + \hat{z}) \end{aligned} \tag{3}$$

where the angle $\phi_t = \tan^{-1}(y_t/x_t)$. The incident fields produced by this source can be calculated as

$$\vec{E}^{\mathrm{inc}}_t(\vec{r}) = -j\omega\mu_0 \vec{J}_t \cdot \bar{\bar{G}}(\vec{r}, \vec{r}_t) \tag{4}$$

where the dyadic Green's function for homogeneous medium, $\bar{\bar{G}}(\vec{r}, \vec{r}_t)$, is calculated as

$$\bar{\bar{G}}(\vec{r}, \vec{r}_t) = \left(\bar{\bar{I}} + \frac{\nabla\nabla}{k_b^2} \right) \frac{e^{-jk_b|\vec{r} - \vec{r}_t|}}{4\pi|\vec{r} - \vec{r}_t|}. \tag{5}$$

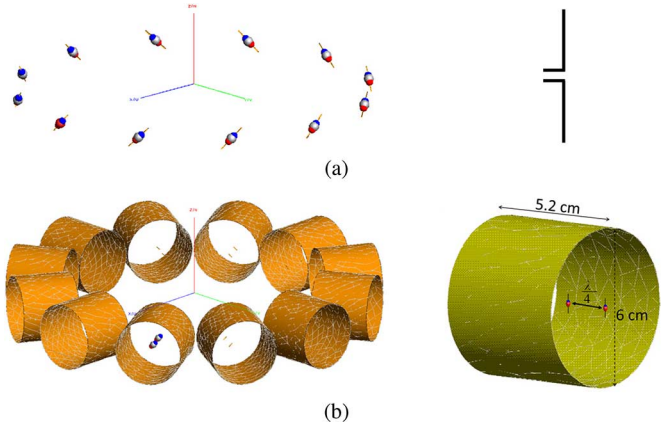

Fig. 5. (a) Slanted dipoles and (b) DFCC antenna system models.

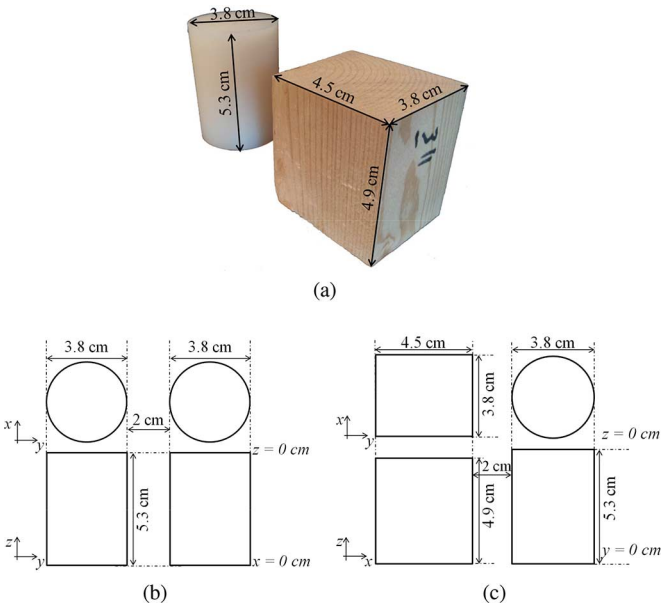

Fig. 6. (a) Nylon cylinder and wooden block objects. (b) Two nylon cylinder OI configuration. (c) Wooden block and nylon cylinder OI configuration.

This incident field model is used for calibrating the data from the system, as well as for the inversion algorithm.

1) Two Nylon Cylinders: The first composite OI consists of two nylon cylinders, whose dimensions and separation are depicted in Fig. 6(a). The cylinders were placed at the center of the imaging chamber. A nylon cylinder is shown in Fig. 6(a). The nylon cylinders are low loss with a relative permittivity $\epsilon_r^{\text{nylon}} \approx 2.7$. The data were collected at a frequency of 3.5 GHz. The real component of the reconstruction results are shown in Fig. 7 at planes $x = 0$, $y = [-3.47, 3.65]$ cm, and $z = 0$. The white solid lines in the figure show the expected location of the objects.

2) Wooden Block/Nylon Cylinder: This composite target consists of a wooden block and a nylon cylinder separated by 2 cm, as shown in Fig. 6(a). The wooden block utilized is shown in Fig. 6(a). The wooden block has a relative permittivity $\epsilon_r^{\text{wood}} \approx 1.9$. The wooden block loss is negligible. The experimental data were collected at 4 GHz. 2-D cross-section plots of the real part reconstruction at planes $x = [-3.8, 4]$ cm, $y = 0$, and $z = 0$ are shown in Fig. 8. The white solid lines in the figure show the expected location of the objects.

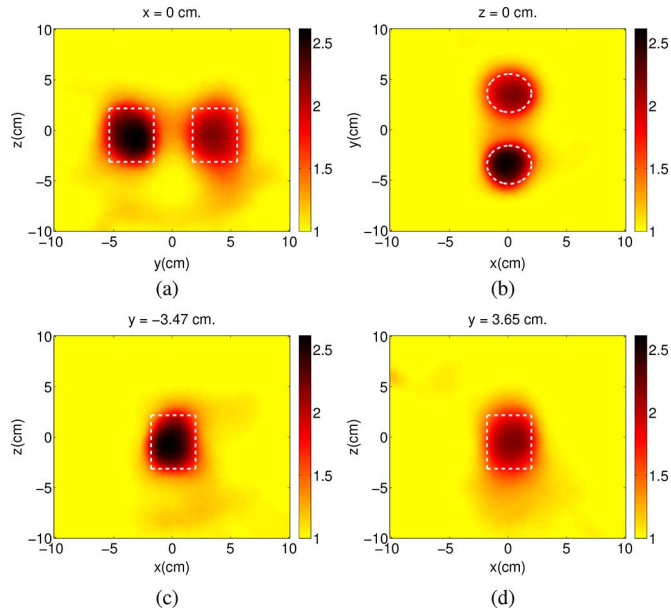

Fig. 7. Reconstructions of two nylon cylinders OI at 3.5 GHz using Hertzian dipole model. The 2-D cross section plots at planes: (a) $x = 0$ cm, (b)$z = 0$ cm, (c) $y = -3.47$ cm, and (d) $y = 3.65$ cm. The white solid lines depict the expected location of the OI.

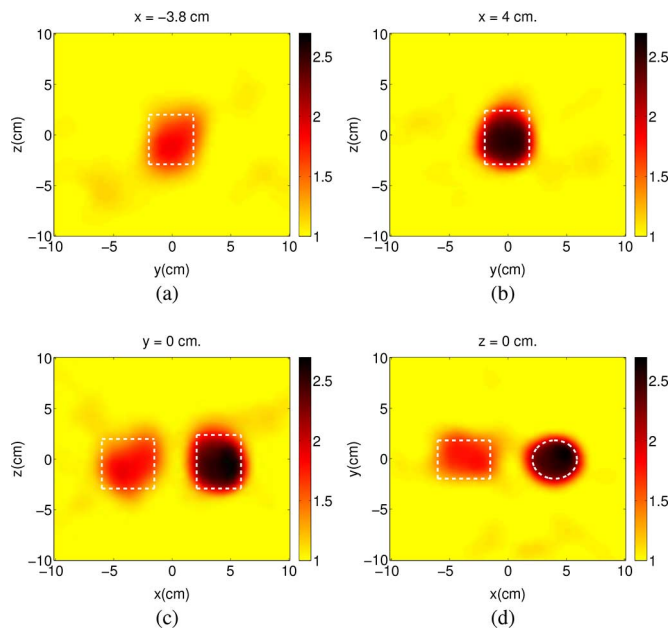

Fig. 8. Reconstructions of wooden block/nylon cylinder OI at 4.0 GHz using Hertzian dipole model. The 2-D cross section plots at planes: (a) $x = -3.8$ cm, (b) $x = 4$ cm, (c) $y = 0$ cm, and (d) $z = 0$ cm. The white solid lines depict the expected location of the OI.

B. Dipole Fed Cylindrical Cavity (DFCC)

One of the challenges in reconstructing an image from the measured dataset is the accurate numerical modeling of the measurement setup, including proper models for the antennas. Generally, the differences between the actual physical setup and the inversion model leads to modeling errors, which can destroy the

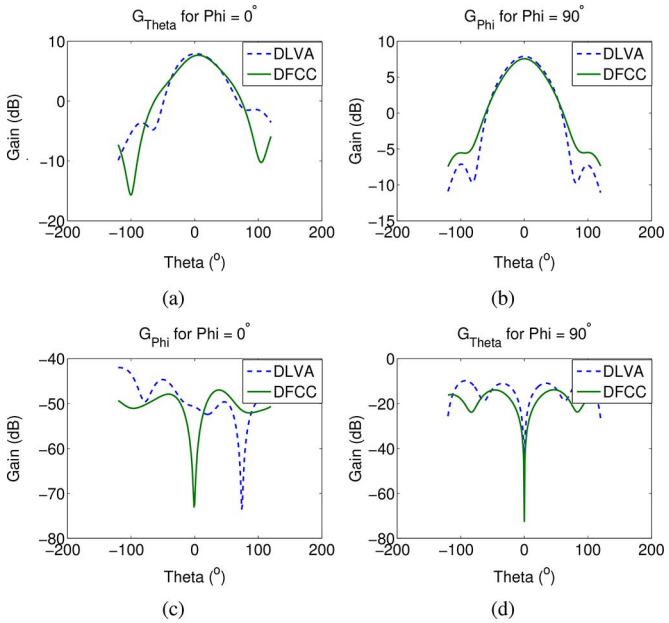

Fig. 9. Comparison between the radiations patterns of the DFCC and the DLVA antennas at 3.5 GHz.

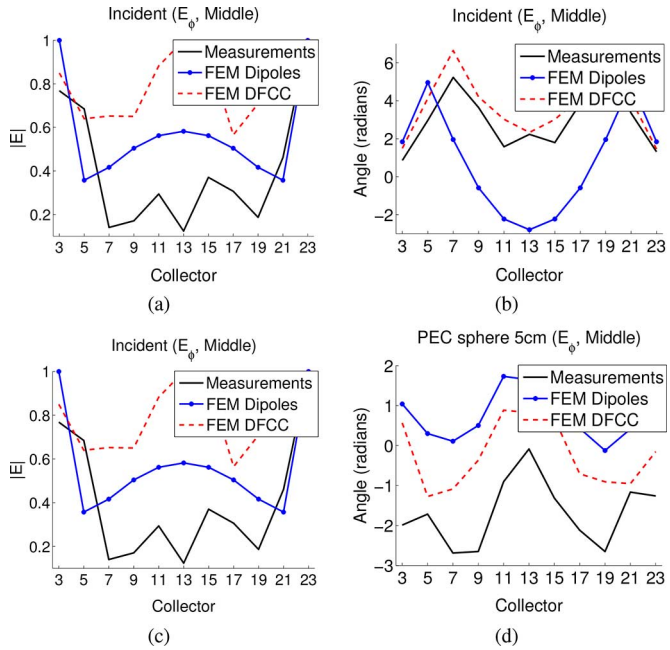

Fig. 10. Comparison at 3.5 GHz between system measurements, and data from the DFCC model and the slanted Hertzian dipole model. (a) and (b) Magnitude and phase of incident field. (c) and (d) Magnitude and phase of scattered field from a PEC object.

nonlinear inversion results. In order to minimize this modeling error, the incorporation of full-wave models, which take into account all of the essential features of the system, would be ideal. However, the complexity of the DLVA-cavity assemblies used in the current system make the inclusion of accurate models for them into the inversion algorithm prohibitive due to the computational resources that would be required.

Even though promising results were obtained using the Hertzian dipole model for the antennas (as shown in Section III-A), the error corresponding to this model is still significant. One of the main reasons for this difference is the omnidirectional pattern of dipoles compared with that of the DLVAs. Furthermore, the cylindrical cavities surrounding the imaging domain and their associated scattering are completely ignored in the Hertzian dipole model.

In order to reduce this error while keeping the system model as simple as possible, the field properties of the DLVA-cavity assemblies are used for the development of a new system model. Knowing the mode distribution inside the cavity, as well as the radiation characteristics of this antenna [30], it was found that two slanted dipoles placed inside a cylindrical cavity separated by $\lambda/4$ and excited uniformly with a 90° phase shift between them can closely approximate the radiation pattern of this antenna. A schematic of this model is shown in Fig. 5(b). The proper location of the dipoles with respect to the center and the opening of the cavity was found using a parametric analysis [32]. The best match between the pattern of the DFCC and the DLVA-cavity assembly was then selected as the model for the data calibration and the inversion algorithm. Fig. 9(b) provides a comparison between the patterns of the proposed DFCC and the DLVA-cavity assembly.

Using these results, the full system was modeled and analyzed. The performance of the proposed DFCC antenna model and the Hertzian dipoles model in comparison to the measurement results is presented in Fig. 10; here one of the antennas is used as the transmitter, while the rest of them are in receiving mode. As can be observed from these results, the difference between the measurement and the simulation model has been reduced when the DFCC model is adopted. The graphs of Fig. 10 show better agreement for phase than for amplitude especially when no object is present in the imaging system. This is consistent with what was reported in [33]. The presence of antennas and probes in close proximity to the object, as well as the near-field nature of such systems, is the main cause of these discrepancies.

1) Wooden Block/Nylon Cylinder Using DFCC: To illustrate the enhancement in the acquired image using the new model, the collected data for the wooden block and nylon cylinder of Fig. 6(a) were inverted with transmitters modeled first as Hertzian dipoles, and then as DFCCs. This was performed at 3.5 GHz. 2-D cross-section plots of the real and imaginary part reconstruction at planes $y = 0$ and $z = 0$ are shown in Fig. 11.

2) Results Discussion: As can be observed from the reconstructions, when the transmitters are modeled using DFCC antennas, the imaginary part of the permittivity is also successfully reconstructed. However, with the antennas modeled as Hertzian dipoles, no meaningful reconstruction of the imaginary part is obtained. Moreover, the real part of the inverted image using the DFCC model is more clear with fewer artifacts in comparison to the Hertzian dipole model.

The results are satisfactory as the inversion algorithm was capable of distinguishing the presence of the two targets per configuration, along with correctly estimating their size and location. In both datasets, the relative electric permittivities were underestimated: $\epsilon_r^{\text{nylon}}$ was estimated at 2.5 instead of 2.7 and ϵ_r^{wood} at 1.5 rather than 1.9. For the wooden block/nylon cylinder dataset, the shape of wooden block in the $y = 0$ plane

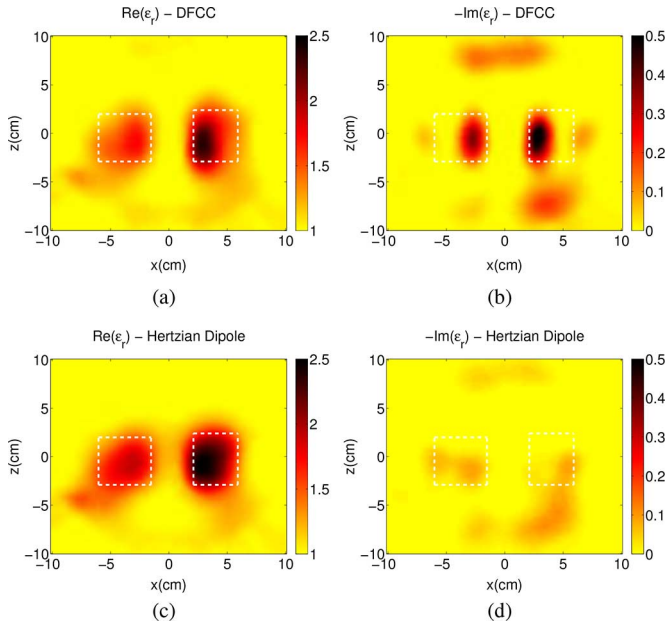

Fig. 11. Reconstructions of wooden block/nylon cylinder OI at 3.5 GHz. The 2-D cross section plots at the $y = 0$ plane for real and imaginary part of the permittivity using DFCC and slanted dipoles. The white solid lines depict the expected location of the OI.

is not rectangular; this might be due to the limited amount of data available to perform the inversion. Other contributing error factors are modeling error in the incident field considered and the assumed location and size of the calibration object. Nevertheless, the modeling error was reduced up to some extent by adopting a DFCC antenna model rather than a simplistic Hertzian dipole model. The effect of modeling error reduction was more significant in the imaginary part of the inverted permittivity.

IV. Conclusion

In this paper, we have presented an MST-based 3-D full-vectorial multiple polarization MWI system. The system was successfully tested and numerical results have shown successful inversion of experimental datasets. To enhance the inversion results, the modeling error of the system was reduced by adopting a DFCC antenna model. The main advantage of this model was the reduced complexity of the experimental system model.

Acknowledgment

The authors acknowledge the help of Z. Trajkoski and C. Smit for their assistance in fabricating parts of the measurement setup.

References

[1] A. Franchois and C. Pichot, "Microwave imaging-complex permittivity reconstruction with a Levenberg–Marquardt method," *IEEE Trans. Antennas Propag.*, vol. 45, no. 2, pp. 203–215, Feb. 1997.

[2] N. Joachimowicz, C. Pichot, and J.-P. Hugonin, "Inverse scattering: An iterative numerical method for electromagnetic imaging," *IEEE Trans. Antennas Propag.*, vol. 39, no. 12, pp. 1742–1753, Dec. 1991.

[3] M. Benedetti, M. Donelli, A. Martini, M. Pastorino, A. Rosani, and A. Massa, "An innovative microwave-imaging technique for nondestructive evaluation: Applications to civil structures monitoring and biological bodies inspection," *IEEE Trans. Instrum. Meas.*, vol. 55, no. 6, pp. 1878–1884, Dec. 2006.

[4] M. Ostadrahimi, P. Mojabi, A. Zakaria, J. LoVetri, and L. Shafai, "Enhancement of Gauss–Newton inversion method for biological tissue imaging," *IEEE Trans. Microw. Theory Techn.*, vol. 61, no. 9, pp. 3424–3434, Sep. 2013.

[5] S. Semenov, J. Kellam, Y. Sizov, A. Nazarov, T. Williams, B. Nair, A. Pavlovsky, V. Posukh, and M. Quinn, "Microwave tomography of extremities: 1. Dedicated 2-D system and physiological signatures," *Phys. Med. Biol.*, vol. 56, pp. 2005–2017, Mar. 2011.

[6] N. K. Nikolova, "Microwave imaging for breast cancer," *IEEE Microw. Mag.*, vol. 12, no. 7, pp. 78–94, Dec. 2011.

[7] D. M. Sheen, D. L. McMakin, and T. E. Hall, "Three-dimensional millimeter-wave imaging for concealed weapon detection," *IEEE Trans. Microw. Theory Techn.*, vol. 49, no. 9, pp. 1581–1592, Sep. 2001.

[8] M. Ghasr, P. Puleo, and R. Zoughi, "Novel reflectometer for millimeter wave 3-D holographic imaging," in *Proc. IEEE Instrum. Meas. Technol. Conf.*, 2013, pp. 647–651.

[9] M. Pastorino, *Microwave Imaging*. New York, NY, USA: Wiley, 2010, vol. 208.

[10] F. Viani, P. Rocca, G. Oliveri, D. Trinchero, and A. Massa, "Localization, tracking, and imaging of targets in wireless sensor networks: An invited review," *Radio Sci.*, vol. 46, no. 5, 2011.

[11] J. M. Sill and E. C. Fear, "Tissue sensing adaptive radar for breast cancer detection-experimental investigation of simple tumor models," *IEEE Trans. Microw. Theory Techn.*, vol. 53, no. 11, pp. 3312–3319, Nov. 2005.

[12] E. Fear, J. Bourqui, C. Curtis, D. Mew, B. Docktor, and C. Romano, "Microwave breast imaging with a monostatic radar-based system: A study of application to patients," *IEEE Trans. Microw. Theory Techn.*, vol. 61, no. 5, pp. 2119–2128, May 2013.

[13] M. Klemm, I. Craddock, J. Leendertz, A. Preece, and R. Benjamin, "Radar-based breast cancer detection using a hemispherical antenna array-experimental results," *IEEE Trans. Antennas Propag.*, vol. 57, no. 6, pp. 1692–1704, Jun. 2009.

[14] C. Gilmore, P. Mojabi, A. Zakaria, M. Ostadrahimi, C. Kaye, S. Noghanian, L. Shafai, S. Pistorius, and J. LoVetri, "A wideband microwave tomography system with a novel frequency selection procedure," *IEEE Trans. Biomed. Eng.*, vol. 57, no. 4, pp. 894–904, Apr. 2010.

[15] P. M. Meaney, M. W. Fanning, D. Li, S. P. Poplack, and K. D. Paulsen, "A clinical prototype for active microwave imaging of the breast," *IEEE Trans. Microw. Theory Techn.*, vol. 48, no. 11, pp. 1841–1853, Nov. 2000.

[16] A. H. Golnabi, P. M. Meaney, S. Geimer, and K. D. Paulsen, "Microwave imaging for breast cancer detection and therapy monitoring," in *Proc. IEEE Biomed. Wireless Technol., Networks, Sens. Syst. Top. Conf.*, 2011, pp. 59–62.

[17] T. Grzegorczyk, P. Meaney, P. Kaufman, R. di Florio-Alexander, and K. Paulsen, "Fast 3-D tomographic microwave imaging for breast cancer detection," *IEEE Tran. Med. Imag.*, vol. 31, no. 8, pp. 1584–1592, Aug. 2012.

[18] T. Rubæk, O. Kim, and P. Meincke, "Computational validation of a 3-D microwave imaging system for breast-cancer screening," *IEEE Trans. Antennas Propag.*, vol. 57, no. 7, pp. 2105–2115, Jul. 2009.

[19] V. Zhurbenko, T. Rubaek, V. Krozer, and P. Meincke, "Design and realisation of a microwave three-dimensional imaging system with application to breast-cancer detection," *IET Microw. Antennas Propag.*, vol. 4, no. 12, pp. 2200–2211, Jul. 2010.

[20] S. Y. Semenov, A. E. Bulyshev, A. Abubakar, V. G. Posukh, Y. E. Sizov, A. E. Souvorov, P. M. van den Berg, and T. C. Williams, "Microwave-tomographic imaging of the high dielectric-contrast objects using different image-reconstruction approaches," *IEEE Trans. Microw. Theory Techn.*, vol. 53, no. 7, pp. 2284–2294, Jul. 2005.

[21] J. Geffrin and P. Sabouroux, "Continuing with the Fresnel database: Experimental setup and improvements in 3-D scattering measurements," *Inverse Prob.*, vol. 25, no. 2, Feb. 2009, Art. ID 024001.

[22] M. Ostadrahimi, A. Zakaria, J. LoVetri, and L. Shafai, "A near-field dual polarized (TE-TM) microwave imaging system," *IEEE Trans. Microw. Theory Techn.*, vol. 61, no. 3, pp. 1376–1384, Mar. 2013.

[23] J. Richmond, "A modulated scattering technique for measurement of field distributions," *IEEE Trans. Microw. Theory Techn.*, vol. MTT-3, no. 4, pp. 13–15, Jul. 1955.

[24] J. Bolomey and F. Gardiol, *Engineering Applications of the Modulated Scatterer Technique*. Norwood, MA, USA: Artech House, 2001.

[25] J.-C. Bolomey, H. Memarzadeh-Tehran, and J.-J. Laurin, "Optimization of optically and electrically modulated scattering probes for field measurements," *IEEE Trans. Instrum. Meas.*, vol. 63, no. 1, pp. 154–165, Jan. 2014.

[26] S. Caorsi, M. Donelli, and M. Pastorino, "A passive antenna system for data acquisition in scattering applications," *IEEE Antennas Wireless Propag. Lett.*, vol. 1, no. 1, pp. 203–206, 2002.
[27] M. Donelli, "Guidelines for the design and optimization of wireless sensors based on the modulated scattering technique," *IEEE Trans. Instrum. Meas.*, vol. 63, no. 7, pp. 1824–1833, Jul. 2014.
[28] M. Ostadrahimi, P. Mojabi, S. Noghanian, L. Shafai, S. Pistorius, and J. LoVetri, "A novel microwave tomography system based on the scattering probe technique," *IEEE Trans. Instrum. Meas.*, vol. 61, no. 2, pp. 379–390, Feb. 2012.
[29] M. Ostadrahimi, P. Mojabi, C. Gilmore, A. Zakaria, S. Noghanian, S. Pistorius, and J. LoVetri, "Analysis of incident field modeling and incident/scattered field calibration techniques in microwave tomography," *IEEE Antennas Wireless Propag. Lett.*, vol. 10, pp. 900–903, 2011.
[30] M. OstadRahimi, L. Shafai, and J. LoVetri, "Analysis of a double-layered Vivaldi antenna inside a metallic enclosure," *Progr. Electromagn. Res.*, vol. 143, pp. 503–518, 2013.
[31] A. Zakaria, I. Jeffrey, and J. LoVetri, "Full-vectorial parallel finite-element contrast source inversion method," *Progr. Electromagn. Res.*, vol. 142, pp. 463–483, 2013.
[32] M. Asefi, M. Ostadrahimi, J. LoVetri, and L. Shafai, "Analysis of a 3-D microwave imaging system," in *Proc. IEEE Antennas Propag. Soc. Int. Symp.*, Jul. 2013, pp. 608–609.
[33] T. Henriksson, N. Joachimowicz, C. Conessa, and J.-C. Bolomey, "Quantitative microwave imaging for breast cancer detection using a planar 2.45 GHz system," *IEEE Trans. Instrum. Meas.*, vol. 59, no. 10, pp. 2691–2699, Oct. 2010.

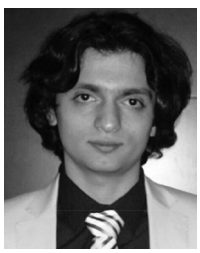

Mohammad Asefi (S'08) received the B.Sc. and M.Sc. degree in antennas and microwave engineering (*cum laude*) from the American University of Sharjah, Sharjah, United Arab Emirates, in 2009 and 2011 respectively, and is currently working toward the Ph.D. degree in electrical engineering at the University of Manitoba, Winnipeg, MB, Canada.

Majid OstadRahimi (S'09–M'12) received the B.Sc. and M.Sc. degrees (with highest distinction) in electrical engineering from the Sharif University of Technology and Iran University of Science and Technology, Tehran, Iran, in 2003 and 2006, respectively, and the Ph.D. degree in electrical and computer engineering from the University of Manitoba, Winnipeg, MB, Canada, in 2011.

He is currently a Post-Doctoral Fellow with the Electromagnetic Imaging Laboratory (EIL), Department of Electrical and Computer Engineering, University of Manitoba. His current main research areas are focused on biomedical imaging, breast cancer detection, design and development of microwave imaging (MWI) systems, near-field measurement, and the modulated scattering technique.

Dr. OstadRahimi was the IEEE Winnipeg Section treasurer (2010 and 2011).

Amer Zakaria (S'05–M'13) received the B.Sc. degree in electrical engineering (*summa cum laude*) from the American University of Sharjah, Sharjah, United Arab Emirates, in 2005, the M.Sc. degree in microwave engineering (with high distinction) from the Munich University of Technology, Munich, Germany, in 2007, and the Ph.D. degree in electrical engineering from the University of Manitoba, Winnipeg, MB, Canada, in 2012.

In 2006 and 2007, he was with the RF Verification Department, Infineon Technologies, Munich, Germany. He is currently a Postdoctoral Fellow with the Department of Electrical and Computer Engineering, University of Manitoba. His research interests include inverse problems, computational electromagnetics, and the development of microwave imaging (MWI) systems.

Joe LoVetri (S'84–M'84–SM'09) received the B.Sc. (with distinction) and M.Sc. degrees in electrical engineering from the University of Manitoba, Winnipeg, MB, Canada, in 1984 and 1987, respectively, the Ph.D. degree in electrical engineering from the University of Ottawa, Ottawa, ON, Canada, in 1991, and the M.A. degree in philosophy from the University of Manitoba, Winnipeg, MB, Canada, in 2006.

From 1984 to 1986, he was an Electromagnetic Interference (EMI)/Electromagnetic Compatibility (EMC) Engineer with the Sperry Defence Division, Winnipeg, MB, Canada. From 1986 to 1988, he was a TEMPEST Engineer with the Communications Security Establishment, Ottawa, ON, Canada. From 1988 to 1991, he was a Research Officer with the Institute for Information Technology, National Research Council of Canada. His academic career began in 1991, when he joined the Department of Electrical and Computer Engineering, The University of Western Ontario, where he remained until 1999. In 1997 and 1998, he spent a sabbatical year with the TNO Physics and Electronics Laboratory, The Hague, The Netherlands, during which time he was involved with time-domain computational methods and ground penetrating RADAR. In 1999, he joined the University of Manitoba, where he is currently Head of the Department of Electrical and Computer Engineering. From 2004 to 2009, he was the Associate Dean (Research and Graduate Programs) for the Faculty of Engineering. His main research interests are in the areas of time-domain computational electromagnetics, modeling of electromagnetic compatibility problems, inverse problems, and biomedical imaging.

Dr. LoVetri has been a Registered Professional Engineer in the Province of Ontario since 1994. From 2005 to 2009, he was the national representative for Commission E on the Canadian National Committee of URSI. In 2010, he cochaired the Ultrawideband and Short-Pulse Electromagnetics Conference, which was part of AMEREM 2010, Ottawa, On, Canada. He has been chapter chair for the IEEE EMC Ottawa Chapter, as well as the Winnipeg Waves Chapter (AP/MTT). He was the recipient of the 1993 URSI Young Scientist Award, the 2000 IEEE EMC Best Symposium Paper Award, and the 2007 ACES Outstanding Paper Award. In 2002, he was the recipient of the University of Manitoba Rh Award for Outstanding Contributions to Scholarship and Research in the Applied Sciences.